Applied Catalysis A, General 692 (2025) 120108

Contents lists available at ScienceDirect

Applied Catalysis A, General

journal homepage: www.elsevier.com/locate/apcata

Long-term stability of Au nanoparticles on rutile-like $Ti_{1-x}Fe_xO_2$ solid solutions for low-temperature CO oxidation

Franklin J. Méndez [a], Alejandro Herrera-González [a], Antonio Morales [a], Carlos Ángeles-Chávez [b], Amado F. García-Ruiz [c], Elim Albiter [d], Dora A. Solís-Casados [e], Xim Bokhimi [a,*]

[a] Instituto de Física, Universidad Nacional Autónoma de México, Ciudad Universitaria, Coyoacán, Ciudad de México 04510, México
[b] Instituto Mexicano del Petróleo, Eje Central Lázaro Cárdenas 152, Ciudad de México 07730, México
[c] Unidad Profesional Interdisciplinaria de Ingeniería y Ciencias Sociales y Administrativas, Instituto Politécnico Nacional, Av. Té 950, Granjas México, Iztacalco, Ciudad de México 08400, México
[d] Escuela Superior de Ingeniería Química e Industrias Extractivas, Instituto Politécnico Nacional, Gustavo A. Madero, Ciudad de México 07738, México
[e] Centro Conjunto de Investigación en Química Sustentable UAEM-UNAM, Universidad Autónoma del Estado de México, Toluca 50200, México

ARTICLE INFO

Keywords:
Au NPs
CO oxidation
Density functional theory
Fe-doped catalysts
Long-term aging
Solid solutions

ABSTRACT

Rutile and Fe-doped rutile were synthesized at low temperatures to support Au NPs. Selected samples were characterized using XRD, SEM-EDS, HRTEM, STEM-HAADF, H_2-TPR, XPS, FTIR and DRIFT spectroscopy of adsorbed CO molecules. To enrich the interpretation, we performed DFT calculation on clusters of rutile, Fe-doped rutile and metallic gold interacting with CO molecules. Catalysts were tested in the CO oxidation reaction, focusing on the roles of activation-reaction time, Au loading, Fe-modification, and long-term aging on performance. Au-based Fe-doped rutile exhibited superior activity compared to the unmodified rutile catalyst. Long-term aging resulted in catalyst deactivation, but reactivation under hydrogen restored the high activity levels. Fe incorporation into rutile promoted the stabilization of the Au NPs by increasing the number of oxygen atoms on the surface, which act as pinning centers. This stabilization prevented the mobility and growth of the Au NPs, improving their dispersion.

1. Introduction

Air pollution is one of the most serious threats, causing great harm to human health and natural resources. Carbon monoxide (CO) is hazardous to health, as it can lead to various problems, including respiratory and cardiovascular disease, and significantly increases the risk of lung cancer [1]. Even at very low concentrations, as small as 1 %, this gas can kill a person by binding tightly to hemoglobin in blood cells, displacing oxygen molecules [2]. As a result, global initiatives have been proposed to reduce CO emissions [3]. However, these emissions have steadily increased due to the growing number of cars with automatic transmissions, which are less efficient than those with manual transmissions [4]. As a result, air pollution from CO will continue to be a significant problem. This issue is exacerbated by the fact that the majority of CO emissions occur during cold starts and short trips, when the internal combustion engine is not fully warmed up [5].

Catalytic converter technologies based on more efficient catalysts that operate at lower temperatures or optimize their placement in the exhaust system can significantly reduce CO emissions by promoting more complete fuel combustion, especially during cold starts [5,6]. In this regard, several catalysts have been developed for low-temperature CO oxidation, particularly those based on supported noble metals such as Pt [7,8], Pd [9,10], Ir [11], Rh [12], Ru [12,13], and Au [14–18]. Among these, since Haruta et al. [14] reported the high catalytic activity of Au NPs, these catalysts have emerged as the most promising for this application.

Au-based catalysts have demonstrated remarkable chemical stability but are susceptible to long-term aggregation, primarily due to particle migration, coalescence, and Ostwald ripening under varying temperature and other reaction conditions [19]. Since their reactivity is highly dependent on particle size [20,21], many methods have been explored to stabilize them, including colloidal methods [22], addition of a second metal [23], peptide-mediated reduction and stabilization [24], and formation of strong covalent metal-support interactions [25]. The most

* Corresponding author.
E-mail address: bokhimi@fisica.unam.mx (X. Bokhimi).

https://doi.org/10.1016/j.apcata.2025.120108
Received 6 November 2024; Received in revised form 3 January 2025; Accepted 4 January 2025
Available online 9 January 2025

commonly used supports for stabilizing and dispersing Au NPs include Al_2O_3 [26], CeO_2 [27,28], and the different polymorphs of TiO_2 [14,29,30]. Among these, TiO_2 is one of the most promising, although its industrial applications remain limited [30].

The selection of TiO_2 polymorphs or their mixtures also appears to be a crucial factor in the activity of Au/TiO_2 catalysts. Tada et al. [31] demonstrated that the catalytic activities of Au/TiO_2 catalysts are identical across different TiO_2 crystal structures when the Au loadings and average particle diameters are the same. However, Beck et al. [32] reported that, despite having smaller Au NPs on brookite support, the CO oxidation activity was unexpectedly higher compared to using anatase as the support. This increase in activity is likely due to differences in the interfaces formed between the Au particles and the support. On the other hand, Di et al. [33] found that the highest performance was achieved with an Au/TiO_2 catalyst having an anatase-rutile ratio of 4:6. This was attributed to the phase transformation mechanism and the preferential deposition of Au NPs on rutile [33,34]. Additionally, Bokhimi et al. [35] demonstrated a direct relationship between the size of the Au particles and the rutile TiO_2 crystallite size, showing that smaller support crystallites resulted in smaller Au NPs and more active catalysts.

Au NPs supported on Fe-modified TiO_2 have demonstrated good activity for CO oxidation. Luengnaruemitchai et al. [36] observed that the Au/Fe_2O_3-TiO_2 catalyst exhibited higher preferential CO conversion compared than Au/Fe_2O_3 and Au/TiO_2 analogues, which is consistent with the findings of Parida et al. [37] and Shou et al. [38]. All these studies reported a significant improvement in catalytic activity with a high Fe oxide loading. However, in most cases, Fe was incorporated by impregnation, which only allows for superficial Fe incorporation, probably forming Fe_2O_3 nanoparticles. As an alternative, the present study used rutile-like $Ti_{1-x}Fe_xO_2$ solid solutions, synthesized at low temperatures, as Au-based catalyst support. These solid solutions stabilized Au NPs for long-term aging up to 15-months. Furthermore, we investigated the role of Au and Fe in the aging-reactivation processes, the activity and stability of the catalyst during CO oxidation, as well as the influence of the activation-reaction time.

2. Experimental

2.1. Reagents

Hydrochloric acid (HCl, 36.5–38.0 %) and urea ($CO(NH_2)_2$, 99.1 %) were supplied by Baker Analyzed®. Titanium (IV) butoxide ($Ti[O(CH_2)_3CH_3]_4$, reagent grade 97 %), iron (III) chloride hexahydrate ($FeCl_3{\cdot}6\ H_2O$, ACS reagent, 98.0–102 %), and tetrachloroauric (III) acid trihydrate ($HAuCl_4{\cdot}3\ H_2O$, ≥99.9 %) were purchased from Sigma-Aldrich. All chemicals were used as received, without further purification, and all solutions were prepared with deionized water having a resistivity of at least 18.2 MΩ cm^{-1}.

2.2. Synthesis of rutile and Fe-modified rutile supports

A reference sample of pure rutile powder was prepared at low temperatures using a methodology previously reported by Bokhimi's group [29,39,40]. However, certain synthesis parameters were modified to dope rutile with Fe atoms, forming a rutile-like $Ti_{1-x}Fe_xO_2$ solid solution. As previously described [41], approximately 11.32 mL of concentrated HCl solution was added to a three-necked flask reactor containing 23 mL of deionized water at room temperature under constant magnetic stirring. $Ti[O(CH_2)_3CH_3]_4$ was then added dropwise to the solution, followed by the addition of $FeCl_3{\cdot}6\ H_2O$, with the solution stirred for 30 min to ensure a proper homogenization. The concentration of Ti- and Fe-precursors were adjusted to 0.0231 and 0.0010 mol, respectively, to obtain a $Ti_{1-x}Fe_xO_2$ solid solution with $x = 0.04$, corresponding to 4 % mol Fe. The solution was heated to 90 °C and maintained at this temperature for 14 h. A yellow precipitate was formed, which was recovered by complete evaporation at the same temperature. The solid was subsequently washed with deionized water and centrifuged until a pH of approximately 7 was achieved. The color of the rutile powder without Fe doping was white.

2.3. Preparation of supported Au-based catalysts

The deposition-precipitation with urea (DPU) method was used to support metal nanoparticles [29,42,43], targeting nominal loadings ranging from 1 to 5 wt% Au on both unmodified and Fe-modified supports. This method has been demonstrated to be an effective approach for achieving high deposition efficiency and small particle sizes [42]. In a typical experiment, 500 mg of each support, previously dried at 200 °C overnight, was carefully added to the appropriate amounts of $HAuCl_4{\cdot}3\ H_2O$ dissolved in 25 mL of a 4.2 x 10^{-3} M $CO(NH_2)_2$ solution, which had been protected from light to prevent the decomposition of the Au-precursor [15,42]. The temperature gradually increased to 80 °C using an integrated water heating system within a jacketed reactor and maintained at this temperature for 14 h during the DPU process. It is important to highlight that the DPU time was determined from a time study ranging from 2 to 14 h for a specific Au-based catalyst. Subsequently, the solid was separated by centrifugation, washed with deionized water to remove unreacted ions, and finally dried under vacuum at 90 °C for 2 h.

2.4. Samples nomenclature

The **Ti** and **FeTi** symbols represent the rutile TiO_2 and $Ti_{1-x}Fe_xO_2$ supports, respectively. The **xAuTi** and **xAuFeTi** symbols refer to the Ti- and FeTi-supported Au catalysts, with x representing an Au loading in the range of 1–5 wt%.

2.5. Physicochemical characterizations

2.5.1. X-ray powder diffraction

XRPD patterns were collected using a BRUKER D8 Advance diffractometer, operating in Bragg-Brentano geometry (θ-θ configuration) with Cu Kα radiation, a Ni filter, and a detector equipped with 192 silica strips (BRUKER, LynxEye). Diffraction intensities were recorded as a function of the diffraction angle, 2θ, ranging from 20° to 120°, with a 2θ step of 0.0195° and a measurement time of 211 seconds per point. The crystalline structures were refined using the Rietveld method with TOPAS software version 7 [44].

2.5.2. Elemental analysis

The metal concentration and elemental mapping were obtained using an OXFORD-ISIS microanalyzer coupled to a JEOL JSM-5600 LV SEM microscope. Prior to analysis, the Al-based holders containing each sample were carbon-coated.

2.5.3. Transmission electron microscopy

Two selected catalysts were characterized using HRTEM and STEM-HAADF with a JEOL JEM-2010F FASTEM microscope operated at an accelerating voltage of 200 kV. The particle size distributions were obtained by counting more than 500 particles.

2.5.4. Temperature-programmed reduction

The H_2-TPR profiles were obtained using a MICROMERITICS AUTOCHEM II 2920 automatic analyzer. The reduction process was carried out with a gas flow of 50 mL/min of an Ar/H_2 mixture (90/10 mol/mol), and data were recorded as the temperature increased at a rate of 10 °C/min from room temperature to 800 °C.

2.5.5. X-ray photoelectron spectroscopy

The XPS spectra were acquired using a JEOL JPS-9200 instrument equipped with an Al Kα X-ray source operating at 1486.6 eV. The

spectrometer was set to a pass energy of 20 eV and an X-ray power of 300 W. Charge correction was applied using the C1s signal at 284.8 eV, and curve fitting was performed with the XPS Peak 4.1 software, employing a variable-proportion Gaussian/Lorentzian function after baseline correction using the Shirley method.

2.5.6. *In situ DRIFT spectroscopy of adsorbed CO molecules and conventional FTIR studies*

The interaction between CO and the surface of selected catalysts was studied using a THERMO SCIENTIFIC NICOLET iS50 spectrophotometer equipped with a PIKE DiffusIR DRIFTS cell. The samples were directly introduced into the reaction chamber and subjected to *in situ* pretreatment under the same reduction conditions used during catalytic tests. After reduction, the samples were purged with a He flow while cooling to 25 °C, and then exposed to a 5 % CO/He mixture until saturation. The reaction chamber was purged again, and the spectra were recorded at a resolution of 4 cm^{-1}. Additionally, conventional FTIR spectra were recorded using the same equipment to study the hydroxyl groups while increasing the temperature to 300 °C in the absence of a reactive atmosphere, and to investigate the formation of carbonate species in selected activated, aged, and reactivated catalysts.

2.6. *Catalytic tests*

The Au NPs are initially present in the Au^{3+} state [45]. However, it is known that Au^0 state enhances the catalyst's ability to convert CO to CO_2 [35,45]. Therefore, the obtained catalysts were reduced in a fixed-bed-U-reactor under a H_2 flow to a rate of 200 mL/min. The temperature was increased from room temperature to 300 °C at a rate of 1.5 °C/min and maintained at this temperature for 2 h. The subsequent cooling process was carried out under the same atmosphere.

The CO oxidation reactions were studied in a fixed-bed reactor at atmospheric pressure using approximately 100 mg of the activated catalyst. The O_2-CO-He gas mixture was fed into the reactor at a downflow rate of 100 mL/min, consisting of 50 mL (5 % O_2) and 50 mL (5 % CO), both balanced with He. These oxygen-rich conditions facilitated higher CO_2 formation rates and enabled the evaluation of any potential catalytic activity in a controlled and accelerated environment. The reactor was heated at a constant rate of 5 °C/min, and the CO and CO_2 concentrations were determined as the temperature increased, with aliquots taken at random.

The gas mixtures were analyzed at the inlet of the reactor to determine the reference concentration and at the outlet of the reactor to determine the product concentrations at different temperatures. A GOW-MAC gas chromatograph equipped with a CarboSphere 80/100 column (Alltech), a thermal conductivity detector, and Clarity software version 2.6.6.574 (DataApex Ltd) were employed to obtain and process the data.

2.7. *Theoretical calculations*

A rutile cluster, named **ru203**, containing 31 titanium atoms, 100 oxygen atoms, and 72 hydrogen atoms was constructed. Due to the small size of the cluster, its stabilization required the hydroxylation of its surface with OH groups and water molecules, in accordance with the experimental conditions used for synthesizing the supports, which were rich in hydroxyl groups and water. Furthermore, an atomic cluster named **ru203–3Fe** was constructed by replacing three of the Ti atoms with Fe atoms in different atomic surface environments. It was also constructed a gold cluster with 55 Au atoms that was named **Au55**.

Cluster geometries were optimized to their minimum energy using Density Functional Theory (DFT), with the B3LYP functional and the 6–31 g basis set, implemented in the TeraChem code [46]. This functional and basis set were also used to perform molecular dynamics (MD) calculations with spherical boundary conditions on the optimized ru203 and ru203–3Fe clusters, at temperatures of 300 K, 500 K, and 1000 K, each for 5 ps with a time step of 1 fs, using the Bussi-Parrinello thermostat [47].

A new cluster, named ru203–3Fe-8Au, was built and optimized by adding 8 Au atoms to the ru203–3Fe cluster. To this optimized cluster, 19 CO molecules were added randomly, distributed at a distance of 0.5 nm, and MD simulations were performed at 300 K for 5 ps with a time step of 1 fs. Similarly, 19 CO molecules were added, randomly distributed at 0.5 nm, to the Au55 cluster, and MD simulations were performed at 300 K for 5 ps with a time step of 1 fs. From these last MD calculations, after a time of 1 ps, three different frames differing by 2 fs from each other were taken to calculate their infrared spectra using DFT technique with the B3LYP functional and the 6–31 g basis set implemented in the Gaussian 16 code [48]. Similar calculations were performed on a CO molecule. The calculations for the ru203–3Fe-8Au cluster interacting with 19 CO molecules were also attempted, but our server did not have enough resources for doing it. All calculations were carried out on a server equipped with two Xeon Gold 5220 R CPUs, four Tesla A100 GPUs, and 790 GB of RAM.

3. Results and discussion

3.1. *Phase identification*

Figs. 1 and 2 show the XRPD patterns of the 4AuFeTi catalyst as a function of DPU time and the xAuFeTi catalysts as a function of Au loading (x), respectively. The diffractogram of the FeTi support is also included in Fig. 2. All diffractograms exhibit well-resolved peaks at 2θ = 27.48°, 36.08°, 39.13°, 41.34°, 44.04°, 54.35°, 56.62°, 62.75°, 64.23°, 69.59°, and other less intense signals that closely match those in ICDD file 01–071–0650 [49]. These diffraction peaks correspond to the crystallographic planes (110), (101), (200), (111), (210), (211), (220), (002), (310), and (112) of a rutile-like phase. The absence of any Fe-based oxides or metallic phases, or any other TiO_2 polymorphs such as anatase or brookite, indicates the formation of a rutile-like $Ti_{1-x}Fe_xO_2$ solid solution [41]. Furthermore, as shown in Fig. 1, a signal emerges at 2θ = 38.7° for DPU times greater than 6 h, gradually increasing up to 14 h. This signal corresponds to the (111) crystallographic plane of metallic Au nanoparticles. Since this signal is more clearly observed at longer DPU times, a time of 12 h was selected as the catalyst preparation time for the different Au loadings (see Fig. 2).

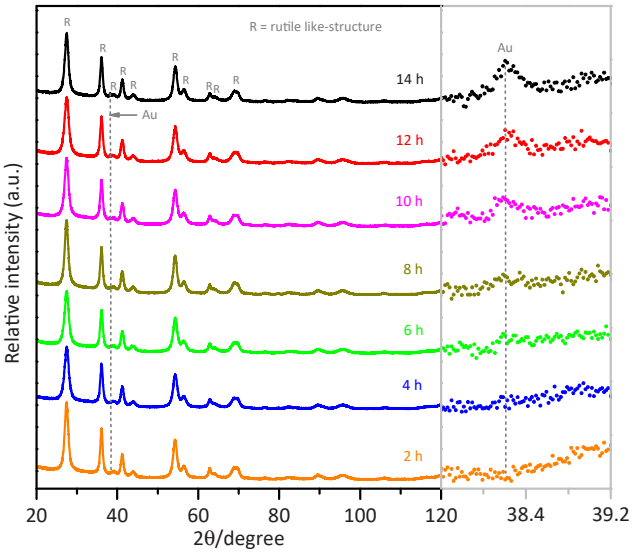

Fig. 1. X-ray powder diffraction patterns of the 4AuFeTi catalyst prepared with different DPU times. The figure also highlights the diffraction region where metallic Au exhibits the strongest diffraction.

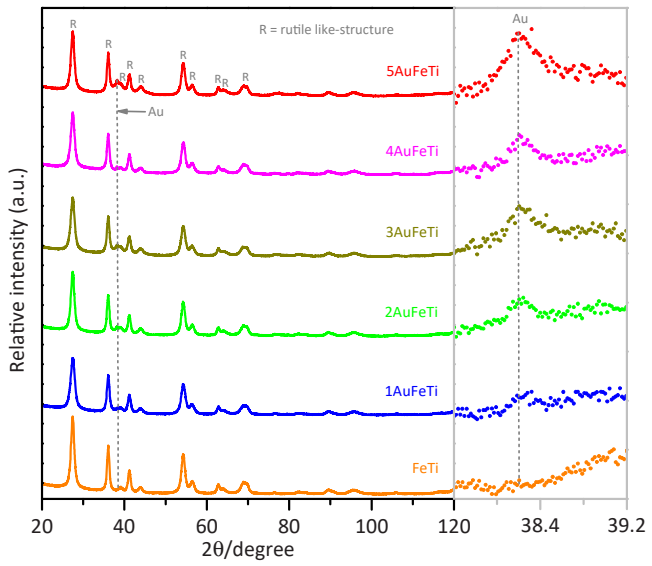

Fig. 2. X-ray powder diffraction patterns of the xAuFeTi catalysts prepared with a DPU time of 14 h and different Au loading. The figure also highlights the diffraction region where metallic Au exhibits the strongest diffraction.

3.2. Quantitative analysis using the Rietveld refinement method

Fig. 3 illustrates the refined patterns of the 4AuFeTi catalyst and its support before the impregnation. The Rietveld refinements for the other Au concentrations are shown in Figure S1 of the Electronic Supporting Information (ESI). The experimental (red lines) and modeled (black lines) diffraction patterns show minimal differences (gray lines).

The refinement shows that the unmodified support has a hexagonal crystalline structure, described by the space group $P4_2/mnm$, with lattice parameters $a = b = 4.6058(3)$ Å, $c = 2.9637(2)$ Å, and $\alpha = \beta = \gamma = 90°$, with the crystal size of the support increasing from 12.3 to 14.9 nm upon Fe incorporation, while the lattice appears to remain unchanged after the Au incorporation [41]. As shown in Table 1, the Au concentrations determined from the refinements were 1.23(4), 2.38(8), 3.56(9), 4.30(9), and 5.53(9) wt% for the xAuFeTi catalysts with x = 1, 2, 3, 4, and 5, which are close to those obtained from the SEM-EDS analysis and consistent with the nominal values. The elemental mapping images also indicated their high dispersion over the support (ESI, Figure S2).

3.3. Nanostructural characteristics

The annular dark-field STEM-HAADF and HRTEM images of two selected catalysts are shown in Fig. 4. All Au NPs appear as bright spots highly dispersed in both supports. Fe incorporation into the rutile structure does not appear to be significantly influence either the Au NPs form or distribution; the NPs had an average particle size of 2.3 ± 0.3 nm (Table 1). Additionally, a detailed HRTEM analysis identified the atomic structures with a high degree of crystallinity, as evidenced by the clearly defined Au NPs, which exhibit an interlayer spacing of 0.213 nm corresponding to the Au(111) plane, supported on the main (110) plane of the rutile structure, with an interlayer spacing of 0.371 nm.

3.4. Reducibility characteristics

The reducibility profiles obtained by the H_2-TPR technique for unmodified and Fe-modified rutile, as well as their respective Au-based catalysts, are shown in Fig. 5. The pure rutile exhibited a single broad and low-intensity signal centered at 568.5 °C, which shifted to 469.9 °C for the Fe-modified rutile support. This signal suggests the reduction of

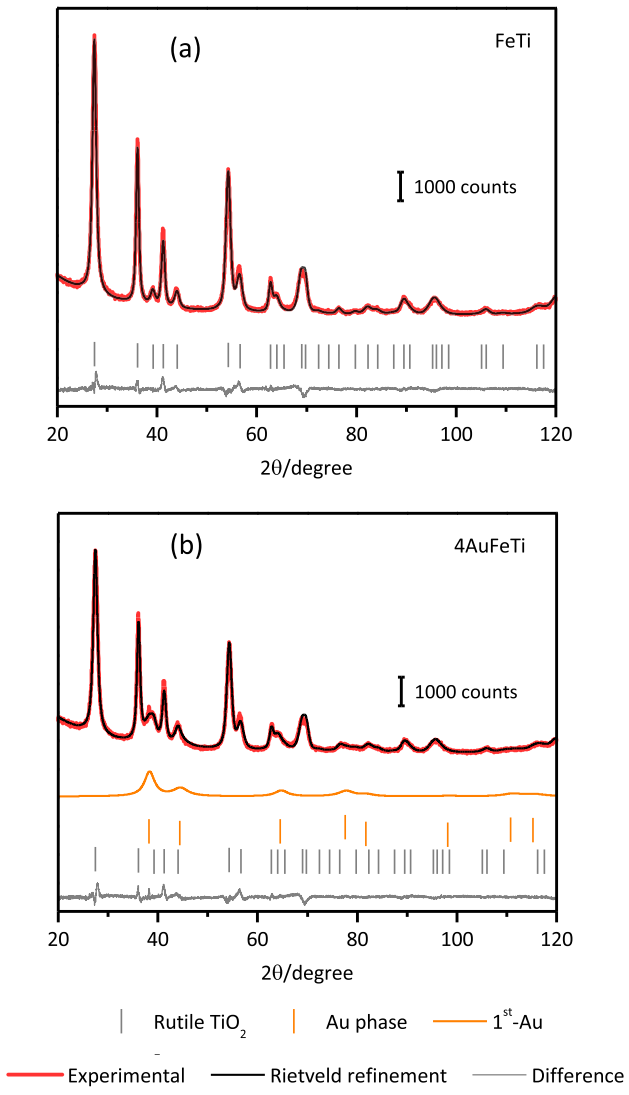

Fig. 3. Rietveld refinement of Fe-modified support (a) and selected Au-based catalyst (b).

Table 1
Au crystallite size, lattice parameter, and elemental composition of selected support and catalysts.

Samples	Crystallite size (nm)	Lattice (Å)	Elemental composition		
			Au (wt%)[a]	Fe (wt%)[b]	Au (wt%)[b]
FeTi				3.74	
1AuFeTi	2.50(9)	4.080(1)	1.23(4)	3.75	1.12
2AuFeTi	2.54(9)	4.101(2)	2.38(8)	3.24	2.54
3AuFeTi	2.36(8)	4.093(2)	3.56(9)	3.25	3.45
4AuFeTi	2.58(7)	4.084(1)	4.30(9)	2.54	5.25
5AuFeTi	2.43(5)	4.080(1)	5.53(9)	3.14	6.14
4AuTi	2.08(7)	4.084(2)	3.57(9)		3.84

Elemental compositions were obtained by Rietveld refinement [a] and SEM-EDS analysis [b].

the titanium atoms near the surface from Ti^{4+} to Ti^{3+} species in both supports [50]. The shifting of the reduction temperature indicates that this transformation is promoted by the presence of the Fe atoms on the surface, which is also observed in our DFT calculations. It is important to mention that when Fe NPs are supported on TiO_2, two signals should appear, corresponding to the successive transformation $Fe_2O_3 \rightarrow FeO \rightarrow Fe$ [51]. However, in the present case, only one peak is observed, likely

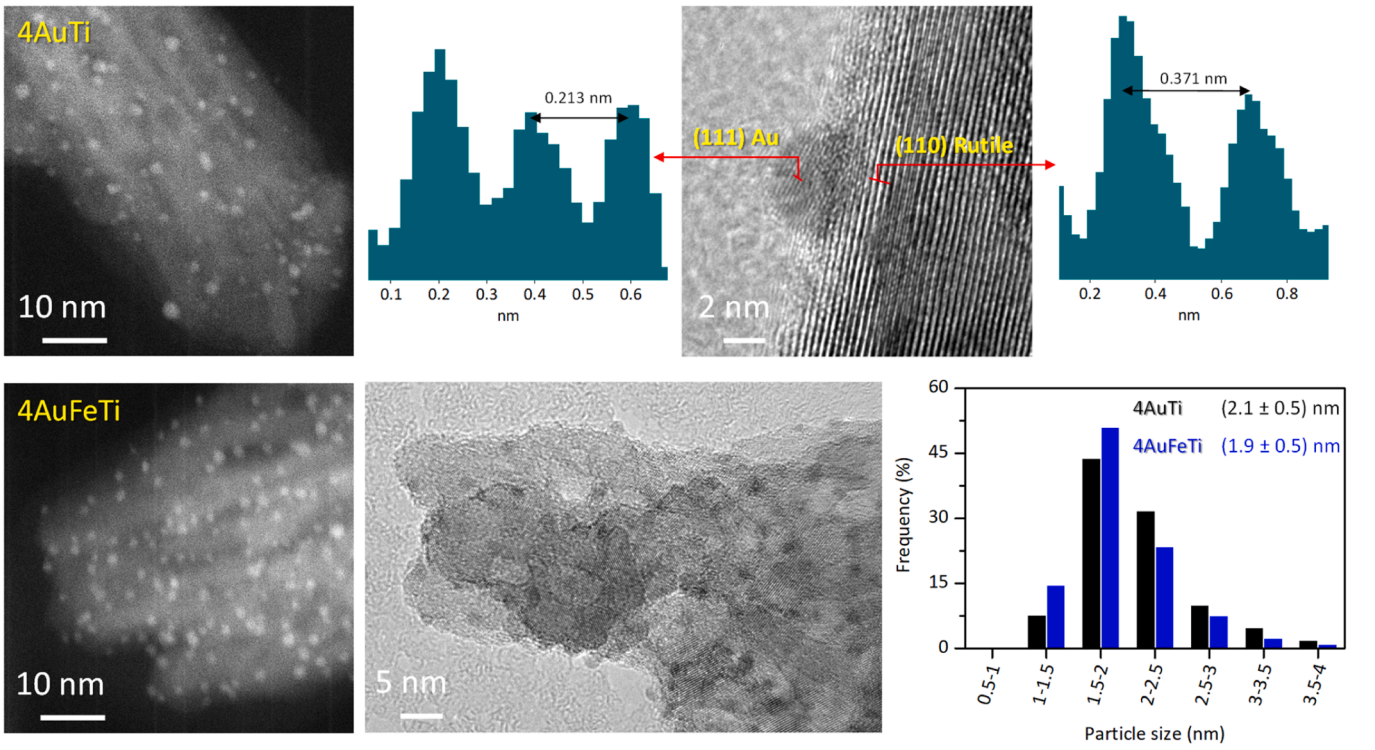

Fig. 4. Representative annular dark-field STEM-HAADF and HRTEM images of two selected catalysts, with particle size distribution and line scan calculated along the red line in the HRTEM image.

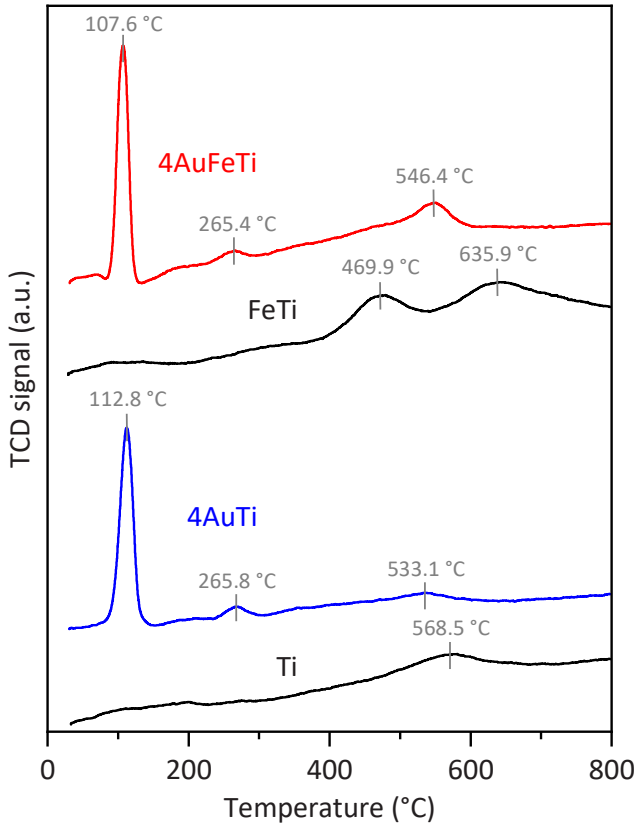

Fig. 5. Reduction profiles of unmodified and Fe-modified supports and Au-based catalysts under a diluted hydrogen flow.

corresponding to the first reduction step from Fe^{3+} species to Fe^{2+}.

The pure rutile-supported Au catalyst exhibited two additional peaks at approximately 112.8 and 265.8 °C, which are associated with the reduction of Au^{3+} species with different degree of aggregation, from the $HAuCl_4 \cdot 3\,H_2O$ precursor to metallic Au^0 species [52]. These reduction temperatures shift to lower values, namely 107.6 and 265.4 °C, respectively, with Fe incorporation. These results indicate that the incorporation of Fe promotes the interaction of the atoms on support surface with Au atoms, leading to an increase in their long-term stability of the AuNPs.

3.5. *Surface species and electronic characteristics*

The surface features of both fresh and reduced Au-based catalysts, derived from the deconvolution of high-resolution Ti2p, O1s, Fe2p, and Au4f XPS spectra, are shown in Fig. 6. In the core-level spectra of the Ti2p region, AuTi and AuFeTi catalysts exhibited $Ti2p_{3/2}$-$2p_{1/2}$ signals at approximately 458.9 eV and 464.6 eV, which are characteristic of the Ti^{4+}-O bond in rutile TiO_2 nanostructures. A notable doublet at 457.0 eV ($Ti2p_{3/2}$) and 462.7 eV ($Ti2p_{1/2}$), indicative of reduced states ($Ti^{\delta+}$), was also observed. The binding energy values for the $Ti^{\delta+}3d_{3/2}$ signals shift from 457.4 to 454.9 eV (AuTi catalyst) and from 457.2 to 456.1 eV (AuFeTi catalyst) upon reduction. These results indicate that the Ti atoms on the rutile surface of our Au-based catalysts are partially reduced, even before the activation process, suggesting a local arrangement of Ti atoms with a low coordination degree in the sub-surface, which is in agreement with the H_2-TPR observations. Additionally, in the core-level spectra of the O1s region, the spectra were resolved into three distinct oxygen environments, with average binding energies of 528.3, 531.8, and 533.3 eV. The first two peaks correspond to the surface ($Ti^{\delta+}$-O) and lattice (Ti^{4+}-O) oxygen species in the rutile TiO_2 nanostructure, while the third signal is attributed to surface -OH groups.

The high-resolution XPS spectra of the Au4f region revealed a single doublet, attributed to the spin-orbit coupling between the $Au4f_{7/2}$ and

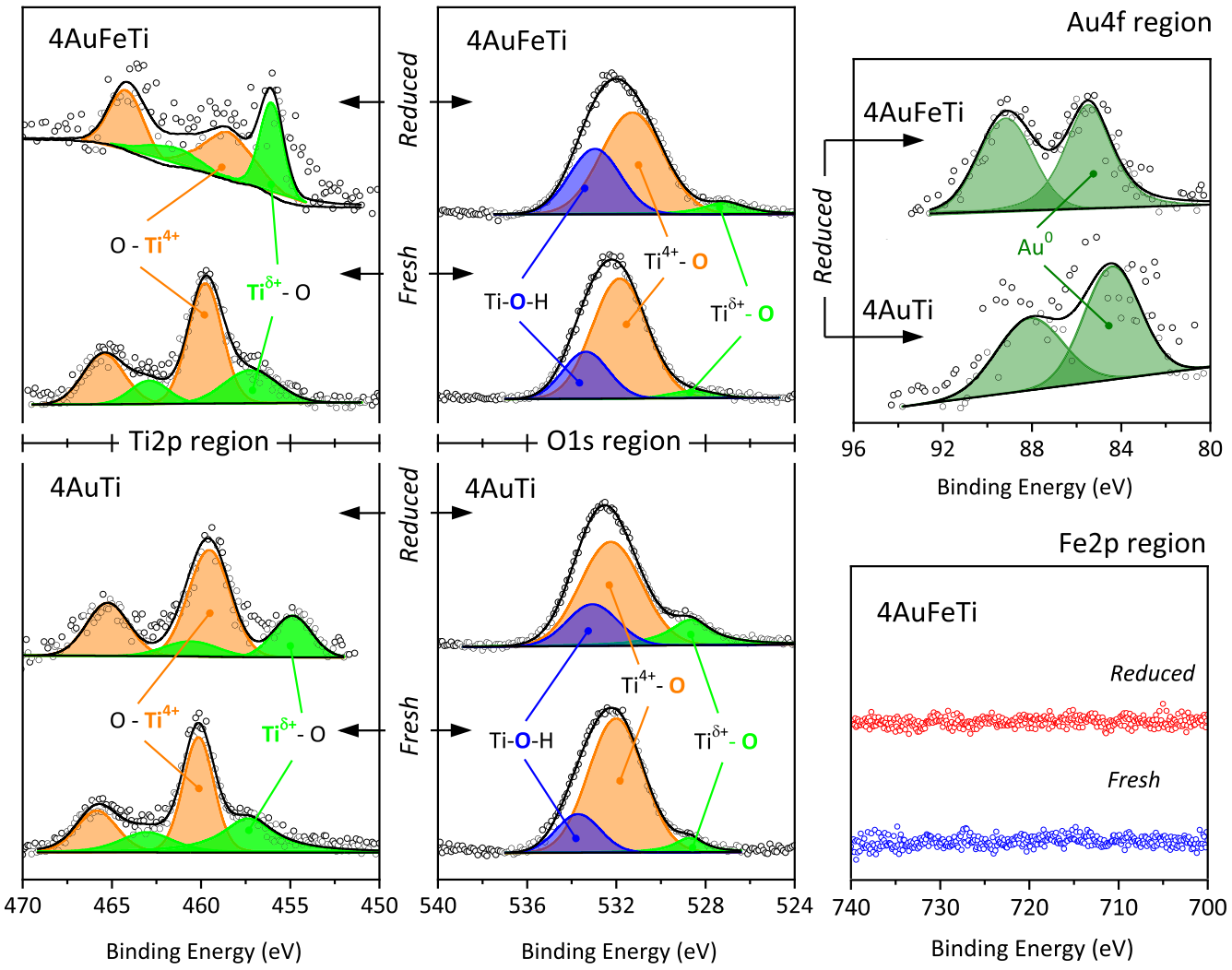

Fig. 6. High-resolution XPS spectra in the Ti2p, O1s, Fe2p, and Au4f regions of unmodified and Fe-modified Au-based catalysts in their fresh and reduced states.

$Au4f_{5/2}$ signals, with an energy separation of approximately 3.7 eV. These signals are associated with reduced Au NPs. A change in the binding energy values was also observed, with shifts from 84.4 to 85.5 eV ($Au4f_{7/2}$) and from 88.1 to 89.2 eV ($Au4f_{5/2}$) after Fe incorporation into the Au-based catalysts. Hinojosa-Reyes et al. [52] suggested that this shift implies a change in the interaction between the Au NPs due to Fe doping in the TiO_2 lattice. Although the XPS results in the Fe2p region do not show any signal, we recently reported, using the more sensitive Mössbauer technique, that Fe atoms co-exist as Fe^{3+} both in the lattice and on the surface [41].

3.6. CO adsorption sites

The adsorption sites on representative *in situ*-reduced Au-based catalysts were studied both under CO flow and after a purging treatment with N_2 flow, ensuring conditions like those of catalytic tests. As shown in Fig. 7a, two signals at approximately 2170 and 2120 cm^{-1} were detected for both samples. Bak and Clausen [53] previously attributed these signals to specific types of rotational transitions within the CO molecule in the gas phase, known as the R and P branches. It is worth noting that the observed peaks disappeared after purging for both Au-based catalysts. Additionally, a pronounced peak at 2110 cm^{-1} was observed, commonly associated with linear carbonyl species adsorbed on low-coordinated sites of Au NPs.

The DFT quantum mechanical calculations showed that the observed IR spectrum does not correspond to the vibrations of two distinct interactions, but rather to an average of the vibrations of CO molecules interacting with Au atoms. These conclusions were obtained after analyzing the molecular dynamics calculations performed at 300 K for the ru203–3Fe-8Au cluster interacting with 19 CO molecules, as well as the corresponding MD of the Au55 cluster also interacting also with 19 CO molecules. In both cases, it is observed that, over time, the CO molecules interact with Au atoms, with bond lengths oscillating around 0.2 nm. Fig. 7b-d show the IR spectra for the Au55 cluster interacting with 19 CO molecules, for three different atomic distributions from the MD calculations, which differ in 2 fs from each other. The IR peak positions change slightly with the atomic distribution and are distributed around the vibration energy of the free CO molecule, which, according to our quantum mechanics calculations, is 2065.56 cm^{-1}. From Table 2 we observe that the CO molecules that do not interact directly with an Au atom have vibration frequencies between 1917.06 and 2279.71 cm^{-1}. This table also shows that the Mulliken charges associated to the Au atoms that directly interact with CO molecules varing from -0.561 to 0.168, dominating the negative values. These values reflect the strength of the interaction between the CO molecules and the Au atoms on the surface.

3.7. CO oxidation tests

To understand how activation-reaction time, Au loading, and long-

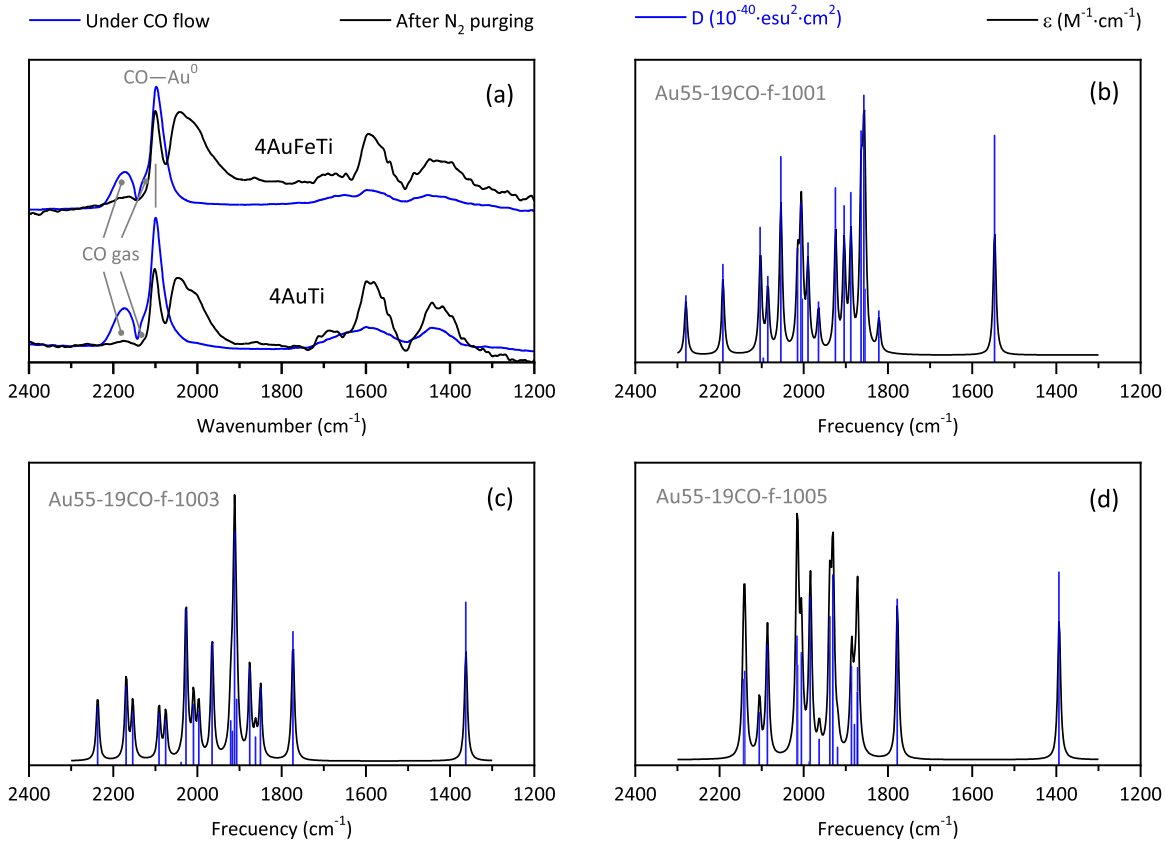

Fig. 7. Experimental *in situ* DRIFT spectra of adsorbed CO molecules on two selected 4AuTi and 4AuFeTi catalysts (a), and theoretical IR spectra of the Au55 cluster interacting with 19 CO molecules after 1 ps for three different atomic distributions (b, c, d), extracted from a Molecular Dynamics Calculation at 300 K. The time between each frame is 2 fs.

term aging affect catalytic performance, CO oxidation was used as a probe reaction to evaluate the xAuFeTi catalyst series. Additional tests were performed with the unmodified xAuTi reference catalyst. The results are expressed as CO conversion as a function of reaction temperature.

3.7.1. *Effect of the activation-reaction time and Au loading*

To study the effect of activation-reaction time on CO oxidation performance, the 1AuFeTi catalyst was selected (Fig. 8a). The sample tested immediately after activation showed higher activity than the test 1-day after activation. Taking this observation into account, all activity tests were performed immediately after the activation of the catalyst.

Fig. 8b shows CO conversion as a function of reaction temperature for selected Au-based catalysts with different Au loadings, including the unmodified 4AuTi reference catalyst; the Au-based catalysts not shown in Fig. 8b are summarized in the ESI file (Figure S3). The 1AuFeTi catalyst achieves a conversion of about 87 % at 23.4 °C and completes conversion at 30.2 °C. This may be due to the low Au concentration in the 1AuFeTi catalyst. Excepting the 1AuFeTi catalyst, a 100 % CO conversion is observed at room temperature for catalysts containing 2 wt% or more Au. Furthermore, all the prepared catalysts, even those with lower Au concentration, exhibited better conversion compared to the reference Fe-free AuTi catalyst (Fig. 8b), which shows a sharp increase in CO conversion in the temperature range from 22.9 to 61.7 °C, followed by a period of total conversion maintained throughout the experiment. These results demonstrate that Fe doping enhances the CO conversion capability of xAuFeTi catalysts even at relatively low Au loading, suggesting that Fe doping may create pinning sites on the rutile support, which act as stabilization centers for the Au NPs.

The DFT calculations on the rutile cluster (left, Fig. 9) and the Fe-doped rutile cluster (right, Fig. 9) show that Au atoms interact with the clusters through oxygen atoms. The number of available oxygen atoms on the surface is larger for the Fe-doped cluster. These calculations suggest that Au particles supported on Fe-doped rutile interact with more oxygen atoms, leading to their stabilization. The DFT calculations also show that, before annealing, the surface of the clusters is rich in hydroxyls, some of which are released as water molecules during annealing. This transformation decreases the number of oxygen atoms on the surface, reducing the valence of surface cations (Ti or Fe). However, the partial transformation of hydroxyls into water molecules also increases the number of oxygen atoms on the surface, enriching the number of pinning centers for Au atoms. The decrease in hydroxyl groups, which was more pronounced in Fe-doped rutile than in undoped rutile, was experimentally confirmed by measuring the Ti–OH stretching vibration at 1630 cm^{-1} using FTIR spectroscopy at different temperatures (Fig. 10).

The DFT MD calculations at 1000 K for 10 fs also show that the presence of Fe atoms in the rutile accelerates the disorder on the cluster surface (Fig. 11). This disorder promotes the reduction of the valence of surface cations (Ti, Fe) and consequently increases the number of oxygen atoms on the surface, which serve as pinning centers for the AuNPs.

3.7.2. *Effect of long-term aging*

Many metal catalysts generally suffer a natural aging process that leads to deactivation over time. This deterioration can occur during the reactions through various mechanisms, such as poisoning by strongly adsorbed species, particle sintering, and leaching of metal and support. Alternatively, catalyst deactivation can also occur during storage due to sintering caused by particle migration. As mentioned earlier, these catalysts are susceptible to aggregation of Au particles over time, mainly due to migration, coalescence, and Ostwald ripening [19]. Although the 2AuFeTi catalyst achieved 100 % CO conversion at room temperature

Table 2
Vibration frequencies (cm^{-1}) of the CO molecules generated using atomic distributions from MD calculations at 300 K for the times 1001, 1003 and 1005 fs. The reported Mulliken charges (e units) correspond to the respective Au atom. The number after the Au symbol corresponds to the Au atom in the Au cluster of 55 atoms. They were used to make the reported results clearer.

Atom	f-1001		f-1003		f-1005	
	Mulliken charge	Freq. (cm^{-1})	Mulliken charge	Freq. (cm^{-1})	Mulliken charge	Freq. (cm^{-1})
Au36-CO	−0.304	1546.67	−0.317	1362.36	−0.345	1393.36
Au1-CO	0.093	1821.50	0.095	1862.00	0.093	1962.94
						1984.28
Au22-CO	−0.260	1854.25	−0.261	1906.92	−0.269	2014.36
				1911.83		2016.05
Au39-CO	−0.561	1854.25	−0.551	1772.94	−0.542	1777.51
Au9-CO	−0.276	1863.60	−0.291	1906.92		1862.94
				1911.83		1984.28
Au24-CO	−0.121	1887.98	−0.123	1850.15	−0.125	1871.66
Au13-CO	0.0690	1903.83	0.059	1875.62	0.046	1886.49
Au32-CO	−0.032	1924.32	−0.033	2009.36	−0.034	2086.17
				2026.96		
Au37-CO	0.101	1964.75	0.102	1996.78	0.101	2005.34
Au34-CO	0.132	1989.75	0.151	1920.99	0.168	1879.28
Au17-CO	−0.346	2006.42	−0.344	1964.86	−0.341	1930.50
Au41-CO	−0.453	2054.21	−0.456	2009.36	−0.458	1937.90
				2026.96		
Au7-CO	0.044	2085.13	0.036	2169.18	0.044	2139.66
Au20-CO	−0.364	2191.66	−0.358	2237.02	−0.341	2142.55
Quasi-free-CO		2003.14		1917.06		1872.72
Quasi-free-CO		2003.14		2075.31		2105.20
Quasi-free-CO		2095.46		2038.95		1986.50
Quasi-free-CO		2103.06		2090.97		2014.31
						2016.06
Quasi-free-CO		2279.71		2153.47		1919.17
						2105.34

(ESI, Figure S3), the 4AuFeTi catalyst was selected for the long-term stability study due to its extraordinary dispersion and the higher possibility of aggregation at increased loading. As described in the previous section, the selected catalyst (magenta solid symbols, Figs. 8b and 12a-b) tested immediately after activation showed nearly 100 % CO conversion at room temperature. However, after aging the catalyst for 2-months (green solid symbols, Fig. 12a), its activity decreased to 67.9 % at room temperature, requiring at least 50 °C to achieve complete CO conversion. After reactivation of the catalyst at 300 °C (green empty symbols, Fig. 12a), it again achieved 100 % CO at room temperature.

A longer aging process (15 months) was also performed on the same catalyst. The 4AuFeTi catalyst experienced greater deactivation, with CO conversion at room temperature decreasing from 100 % for the catalyst tested immediately after activation (magenta solid symbols, Figs. 12b) to 57.8 % for the catalyst tested after 15-months aging (green solid symbols, Fig. 12b). The CO conversion gradually increases with temperature until it reaches 100 % at a reaction temperature of 129.4 °C. Conversely, this aged catalyst recovers its high reactivity after reactivation, achieving 91.5 % conversion at room temperature (green empty symbols, Fig. 12b) and 100 % conversion at 30.2 °C, which is maintained throughout the experiment.

A notable characteristic of the Fe-modified catalyst is their improved resistance to deactivation. Fig. 13 shows the catalytic performance of the 4AuTi catalyst aged for 4 months and the 4AuFeTi catalyst aged for 15-months. At room temperature, the 4AuFeTi catalyst preserves CO conversion close to 57.8 % after 15-months aging (magenta solid symbols, Fig. 13), which is significantly higher than the 14.1 % conversion observed for the 4AuTi catalyst after only 4-months aging (black solid symbols, Fig. 13). Both the 4AuFeTi and 4AuTi catalysts exhibited CO conversion rates close to 100 % at reaction temperatures of

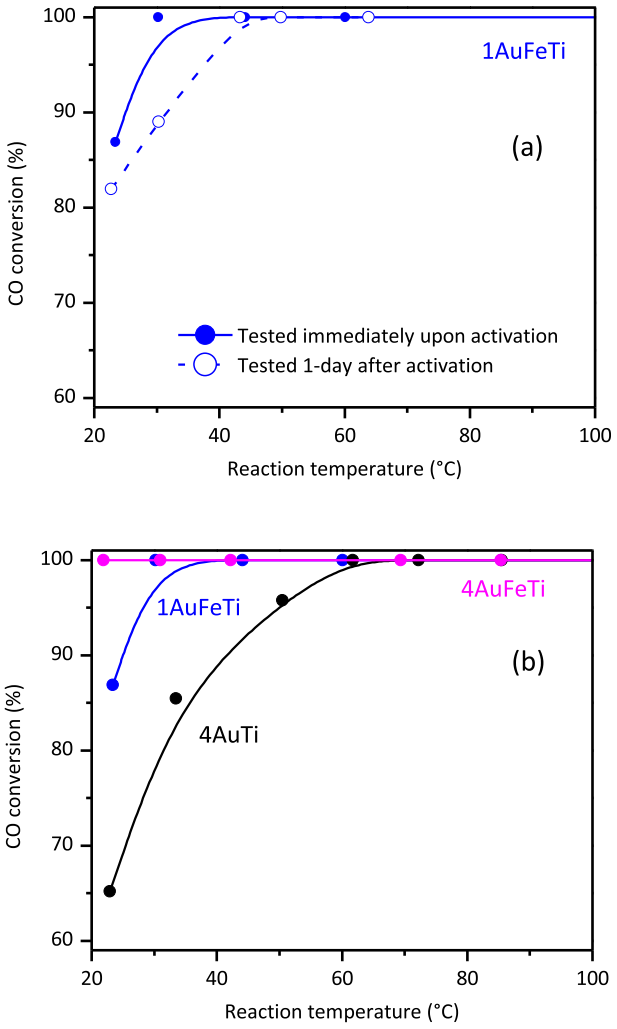

Fig. 8. CO conversion as a function of reaction temperature: Effect of activation-reaction time using the 1AuFeTi catalyst (a), and conversion curves of selected Au-based catalysts with different Au loadings (b).

approximately 102.6 and 129.4°C, respectively.

Fig. 8 indicates that the xAuFeTi catalysts are more active than unmodified xAuTi counterparts. These findings suggest that the Fe atoms act as both promoters and stabilizers of the Au NPs. Furthermore, Fig. 12 shows that the xAuFeTi catalysts experience deactivation over long-term aging. Nevertheless, the data also indicate that these catalysts can be easily reactivated, restoring their high activity levels. After 2-months aging, the reactivated catalyst achieves 100 % CO conversion at room temperature, while the reactivated catalyst aged for 15-months has 91.5 % CO conversion at room temperature. Schumacher et al. [54] previously demonstrated that Au NPs on Au/TiO_2 catalysts are stable during the CO oxidation reaction. However, their activity decreases due to the accumulation of by-products on the surface of the catalysts. Konova et al. [55] identified these by-products as a monolayer of carbonates, which they attributed to a spontaneous oxidation process. The results of the aging and reactivation process suggest that the reactivation procedure is effective in eliminating the deposited compounds that initially reduced the catalyst's effectiveness, as evidenced by the decrease in signals in the interaction zone between the carbonates and the catalyst surface (Fig. 14).

The 4AuTi and 4AuFeTi catalysts exhibited no significant microstructural changes throughout their respective aging processes. Nevertheless, Table 3 shows that the Au particle size, as determined by

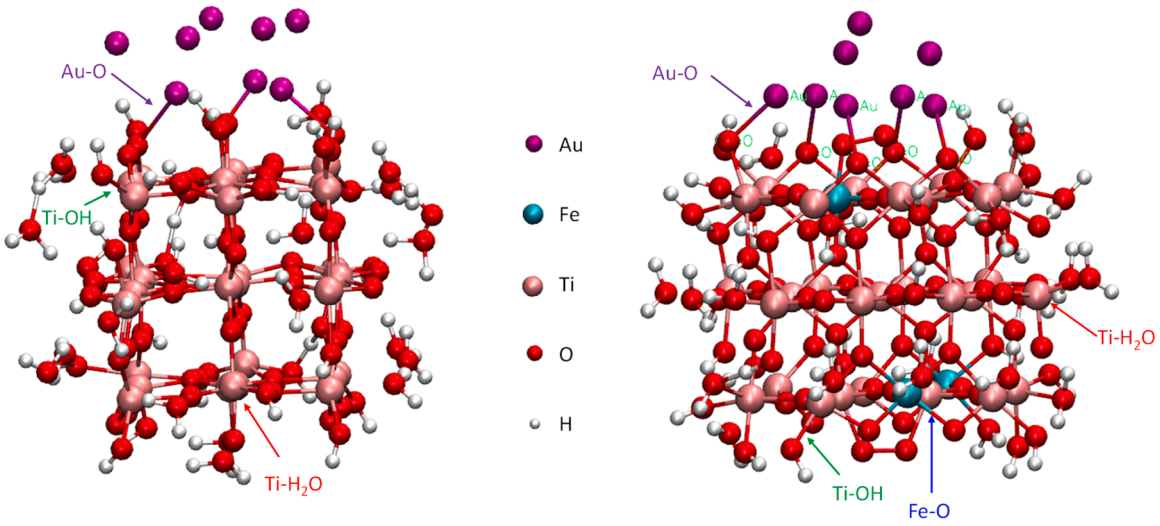

Fig. 9. Atomic cluster ru203–8Au(left) and atomic cluster ru203–3Fe-8Au (right). Because the number of Au atoms in contact with the cluster depends on the number of oxygen atoms in the neighborhood, three Au atoms are attached to the cluster ru203, while five atoms are attached to the cluster ru203–3Fe.

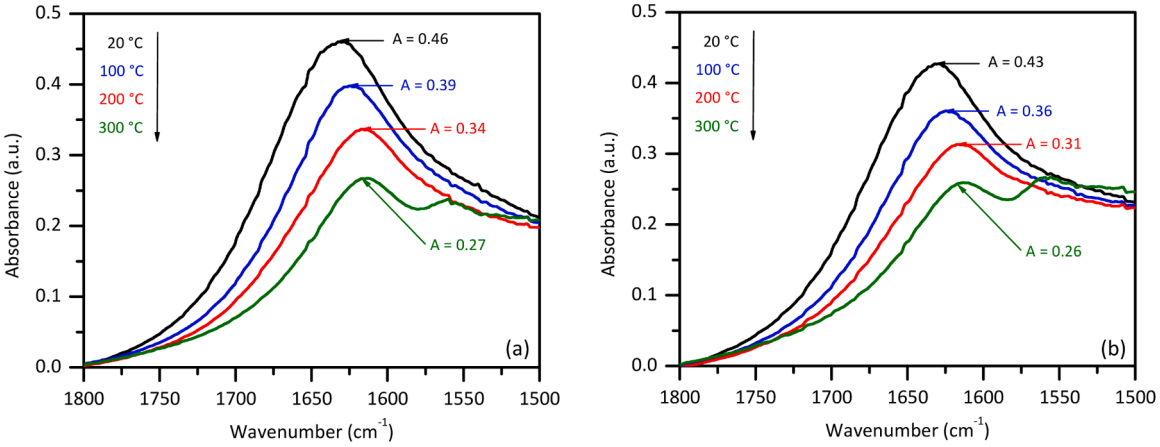

Fig. 10. FTIR spectra of rutile (a) and Fe-doped rutile (b) at different temperatures.

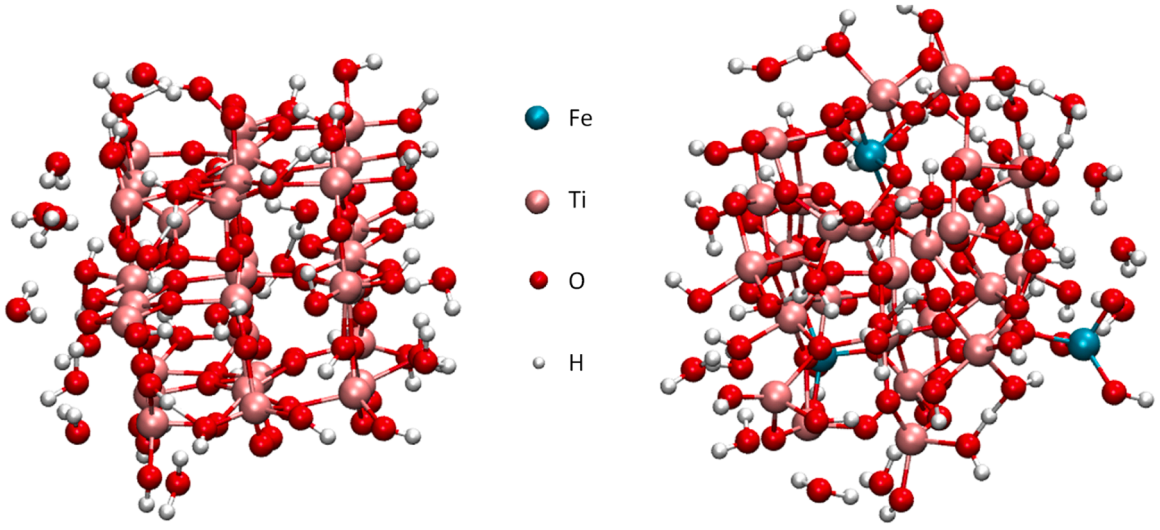

Fig. 11. Atomic clusters after MD at 1000 K for 10 ns: ru203 cluster (left) and ru203–3Fe cluster (right). The figure highlights the effect of Fe in disordering the Ti-O and Fe-O polyhedral on the surface.

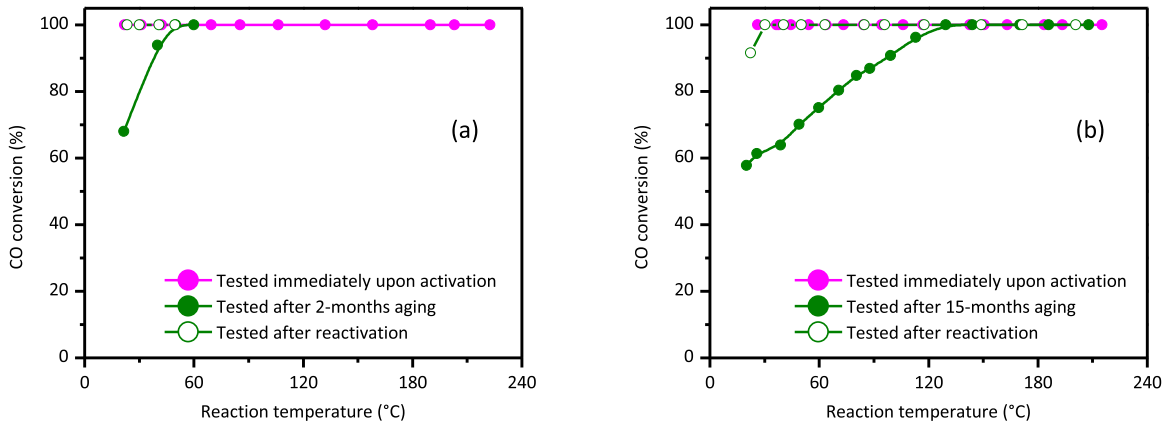

Fig. 12. Effect of long-term aging on CO conversion for a selected 4AuFeTi catalyst. Catalytic tests were carried out after two months (a) and fifteen months (b) post-synthesis, including reactivation tests.

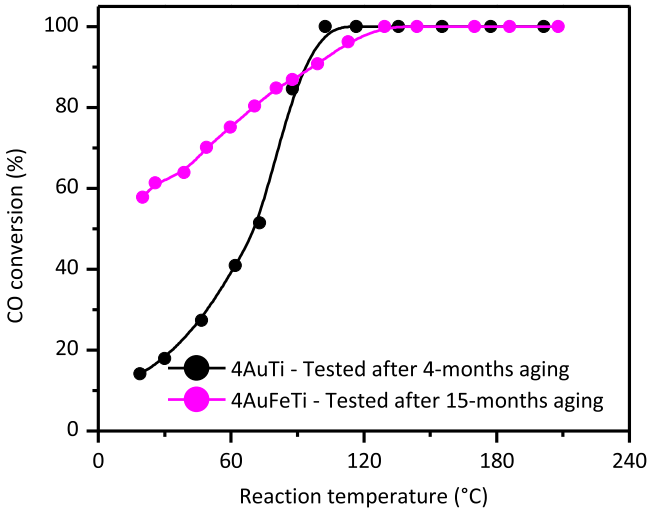

Fig. 13. Effect of Fe-doping on CO conversion after different aging times.

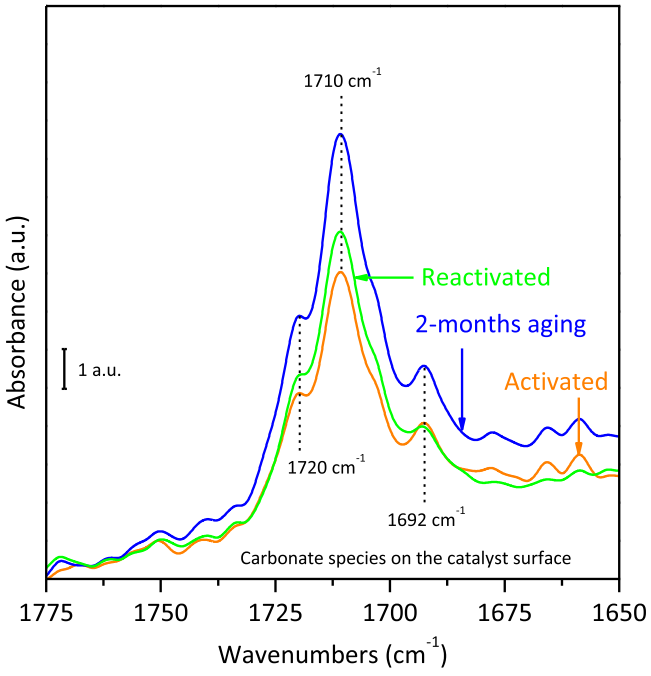

Fig. 14. FTIR spectra of an activated, aged, and reactivated 4AuFeTi catalyst.

Rietveld refinement, increases during this process. The crystal size of the 4AuFeTi catalyst showed a slight increase from 2.6 to 3.8 nm, representing a 1.46-fold increase after 15 months of aging. However, in the unmodified 4AuTi catalyst, the aggregation became more significant after a shorter period of 2 months, with the particle size increasing from 2.1 to 5.3 nm, representing approximately a 2.52-fold aggregation. The observed differences in the growth rate of Au NPs also identified by Konova et al. [55], are factors contributing to the observed decrease in catalytic activity. These factors significantly impact the stability of the catalyst. In any case, this finding indicates that Fe-incorporation into a rutile-like TiO_2 solid solution stabilizes the Au NPs over-term, creating pinning centers that prevent both mobility and growth of Au crystallites, thereby improving the dispersion and stability of the Au NPs.

Table 3
Crystallite size of Au NPs in unmodified and Fe-modified catalysts before and after long-term aging.

Catalysts		Crystallite size (nm)
4AuTi	Tested immediately upon activation	2.1
	Tested after 2-months aging	5.3
4AuFeTi	Tested immediately upon activation	2.6
	Tested after 15-months aging	3.8

4. Conclusions

This study reports how Fe incorporation into the crystalline structure of rutile stabilizes Au NPs during long-term aging. Fe-modified Au catalysts exhibit better CO oxidation activity and stability over-time compared to their unmodified counterparts. Furthermore, although long-term aging leads to the inevitable deactivation of the catalysts, the study also demonstrates that the catalysts can be easily reactivated, restoring high levels of CO conversion. The Au crystallite size increases during the aging process but this effect is more pronounced in the case of the catalyst without iron in the support. The positive effects of Fe-doped catalysts were associated with the creation of pinning centers for the Au NPs, preventing their mobility and growth, and improving their long-term stability. This proposal is supported by quantum mechanical calculations on unmodified and Fe-doped rutile clusters, which shows that the incorporation of iron into rutile promotes the reduction of the cation's valence and the enrichment of oxygen atoms on the surface, which act as the pinning for the Au atoms. Therefore, preparing Fe-based rutile solid solutions as a novel strategy to prepare catalysts for CO oxidation processes mitigates the adverse effects of aging, ensuring a prolonged

activity of the catalysts.

CRediT authorship contribution statement

Xim Bokhimi: Writing – review & editing, Resources, Project administration, Methodology, Investigation, Formal analysis, Conceptualization. **Dora A. Solís-Casados:** Methodology, Investigation. **Elim Albiter:** Methodology, Investigation. **Franklin J. Méndez:** Writing – original draft, Methodology, Investigation, Formal analysis, Data curation, Conceptualization. **Amado García-Ruiz:** Writing – review & editing, Investigation, Formal analysis. **Carlos Ángeles-Chávez:** Investigation, Formal analysis. **Antonio Morales:** Methodology, Investigation, Formal analysis. **Alejandro Herrera-González:** Methodology, Investigation, Formal analysis, Conceptualization.

Declaration of Competing Interest

The authors declare that they have no known competing financial interests or personal relationships that could have appeared to influence the work reported in this paper.

Acknowledgements

This work was financially supported by the LAREC laboratory at the Instituto de Física, Universidad Nacional Autónoma de México. The authors thank R. Hernandez, C. Magaña, and A. Gómez for their technical assistance.

Appendix A. Supporting information

Supplementary data associated with this article can be found in the online version at doi:10.1016/j.apcata.2025.120108.

Data availability

Data will be made available on request.

References

[1] W. Zhang, C.N. Qian, Y.X. Zeng, Air pollution: A smoking gun for cancer, Chin. J. Cancer 33 (2014) 173–175, https://doi.org/10.5732/cjc.014.10034.
[2] I. Blumenthal, Carbon monoxide poisoning, J. R. Soc. Med. 94 (2001) 270–272, https://doi.org/10.1177/014107680109400604.
[3] P. Bielaczyc, Global development of emissions reduction strategies from light duty vehicles, IOP Conf. Ser.: Earth Environ. Sci. 214 (2019) 012139, https://doi.org/10.1088/1755-1315/214/1/012139.
[4] N. Bagameri, B. Varga, A. Csato, D. Moldovanu, Comparative analysis of automatic transmission and manual transmission behaviour on the worldwide harmonized light duty test cycle, MATEC Web Conf. 184 (2018) 01020, https://doi.org/10.1051/matecconf/201818401020.
[5] M.S. Reiter, K.M. Kockelman, The problem of cold starts: A closer look at mobile source emissions levels, Transp. Res. Part D: Transp. Environ. 43 (2016) 123–132, https://doi.org/10.1016/j.trd.2015.12.012.
[6] J. Gao, G. Tian, A. Sorniotti, A.E. Karci, R. Di Palo, Review of thermal management of catalytic converters to decrease engine emissions during cold start and warm up, Appl. Therm. Eng. 147 (2019) 177–187, https://doi.org/10.1016/j.applthermaleng.2018.10.037.
[7] M.A. Newton, D. Ferri, G. Smolentsev, V. Marchionni, M. Nachtegaal, Room-temperature carbon monoxide oxidation by oxygen over Pt/Al_2O_3 mediated by reactive platinum carbonates, Nat. Commun. 6 (2015) 8675, https://doi.org/10.1038/ncomms9675.
[8] I. Kocemba, I. Śmiechowicz, M. Jędrzejczyk, J. Rogowski, J.M. Rynkowski, High catalytic activity of Pt/Al_2O_3 catalyst in CO oxidation at room temperature: A new insight into strong metal-support interactions, Catalysts 11 (2021) 1475, https://doi.org/10.3390/catal11121475.
[9] B. Qiao, L. Liu, J. Zhang, Y. Deng, Preparation of highly effective ferric hydroxide supported noble metal catalysts for CO oxidations: From gold to palladium, J. Catal. 261 (2009) 241–244, https://doi.org/10.1016/j.jcat.2008.11.012.
[10] L. Liu, F. Zhou, L. Wang, X. Qi, F. Shi, Y. Deng, Low-temperature CO oxidation over supported Pt, Pd catalysts: Particular role of FeO_x support for oxygen supply during reactions, J. Catal. 274 (2010) 1–10, https://doi.org/10.1016/j.jcat.2010.05.022.
[11] M. Okumura, N. Masuyama, E. Konishi, S. Ichikawa, T. Akita, CO oxidation below room temperature over Ir/TiO_2 catalyst prepared by deposition precipitation method, J. Catal. 208 (2002) 485–489, https://doi.org/10.1006/jcat.2002.3603.
[12] S. Dey, G.C. Dhal, Applications of rhodium and ruthenium catalysts for CO oxidation: An overview, Polytechnica 3 (2020) 26–42, https://doi.org/10.1007/s41050-020-00023-5.
[13] M.R. Ahasan, R. Wang, CeO_2 nanorods supported CuO_x-RuO_x bimetallic catalysts for low temperature CO oxidation, J. Colloid Interface Sci. 654 (2024) 1378–1392, https://doi.org/10.1016/j.jcis.2023.10.113.
[14] M. Haruta, S. Tsubota, T. Kobayashi, H. Kageyama, M.J. Genet, B. Delmon, Low-temperature oxidation of CO over gold supported on TiO_2, α-Fe_2O_3, and Co_3O_4, J. Catal. 144 (1993) 175–192, https://doi.org/10.1006/jcat.1993.1322.
[15] G.C. Bond, D.T. Thompson, Catalysis by gold, Catal. Rev. 41 (1999) 319–388, https://doi.org/10.1081/CR-100101171.
[16] B.K. Min, C.M. Friend, Heterogeneous gold-based catalysis for green chemistry: Low-temperature CO oxidation and propene oxidation, Chem. Rev. 107 (2007) 2709–2724, https://doi.org/10.1021/cr050954d.
[17] X.Y. Liu, A. Wang, T. Zhang, C.-Y. Mou, Catalysis by gold: New insights into the support effect, Nano Today 8 (2013) 403–416, https://doi.org/10.1016/j.nantod.2013.07.005.
[18] M. Sankar, Q. He, R.V. Engel, M.A. Sainna, A.J. Logsdail, A. Roldan, D.J. Willock, N. Agarwal, C.J. Kiely, G.J. Hutchings, Role of the support in gold-containing nanoparticles as heterogeneous catalysts, Chem. Rev. 120 (2020) 3890–3938, https://doi.org/10.1021/acs.chemrev.9b00662.
[19] V. Sudheeshkumar, C. Soong, S. Dogel, R.W.J. Scott, Probing the thermal stability of (3-mercaptopropyl)-trimethoxysilane-protected Au25 clusters by *In Situ* transmission electron microscopy, Small 17 (2021) 2004539, https://doi.org/10.1002/smll.202004539.
[20] A. Alshammari, A. Köckritz, V.N. Kalevaru, A. Martin, Influence of precursor on the particle size and stability of colloidal gold nanoparticles, Stud. Surf. Sci. Catal. 175 (2010) 409–412, https://doi.org/10.1016/S0167-2991(10)75072-2.
[21] M. Irfan, M. Moniruzzaman, T. Ahmad, O.Y. Osman, P.C. Mandal, S. Bhattacharjee, M. Hussain, Stability, interparticle interactions and catalytic performance of gold nanoparticles synthesized through ionic liquid mediated oil palm leaves extract, J. Environ. Chem. Eng. 6 (2018) 5024–5031, https://doi.org/10.1016/j.jece.2018.07.031.
[22] J. Zhou, J. Ralston, R. Sedev, D.A. Beattie, Functionalized gold nanoparticles: Synthesis, structure and colloid stability, J. Colloid Interface Sci. 331 (2009) 251–262, https://doi.org/10.1016/j.jcis.2008.12.002.
[23] C. Wan Han, P. Majumdar, E.E. Marinero, A. Aguilar-Tapia, R. Zanella, J. Greeley, V. Ortalan, *In situ* environmental TEM and DFT studies on the highly stable AuIr bimetallic catalyst, Microsc. Microanal. 21 (2015) 569–570, https://doi.org/10.1017/S1431927615003645.
[24] C.J. Munro, M.R. Knecht, Solution effects on peptide-mediated reduction and stabilization of Au nanoparticles, Langmuir 33 (2017) 13757–13765, https://doi.org/10.1021/acs.langmuir.7b01896.
[25] B. Qiao, J.-X. Liang, A. Wang, C.-Q. Xu, J. Li, T. Zhang, J.J. Liu, Ultrastable single-atom gold catalysts with strong covalent metal-support interaction (CMSI), Nano Res. 8 (2015) 2913–2924, https://doi.org/10.1007/s12274-015-0796-9.
[26] N. Masoud, T. Partsch, K.P. de Jong, P.E. de Jongh, Thermal stability of oxide-supported gold nanoparticles, Gold. Bull. 52 (2019) 105–114, https://doi.org/10.1007/s13404-019-00259-9.
[27] H.Y. Kim, H.M. Lee, G. Henkelman, CO oxidation mechanism on CeO_2-supported Au nanoparticles, J. Am. Chem. Soc. 134 (2012) 1560–1570, https://doi.org/10.1021/ja207510v.
[28] H. Ha, S. Yoon, K. An, H.Y. Kim, Catalytic CO oxidation over Au nanoparticles supported on CeO_2 nanocrystals: Effect of the Au-CeO_2 interface, ACS Catal. 8 (2018) 11491–11501, https://doi.org/10.1021/acscatal.8b03539.
[29] X. Bokhimi, R. Zanella, Crystallite size and morphology of the phases in Au/TiO_2 and Au/Ce-TiO_2 catalysts, J. Phys. Chem. C. 111 (2007) 2525–2532, https://doi.org/10.1021/jp066635n.
[30] R.E. Tankard, F. Romeggio, S.K. Akazawa, A. Krabbe, O.F. Sloth, N.M. Secher, S. Colding-Fagerholt, S. Helveg, R. Palmer, C.D. Damsgaard, J. Kibsgaard, I. Chorkendorff, Stable mass-selected $AuTiO_x$ nanoparticles for CO oxidation, Phys. Chem. Chem. Phys. 26 (2024) 9253–9263, https://doi.org/10.1039/D4CP00211C.
[31] K. Tada, Y. Maeda, H. Koga, M. Okumura, TiO_2 crystal structure dependence of low-temperature CO oxidation catalyzed by Au/TiO_2, Chem. Lett. 47 (2017) 200–203, https://doi.org/10.1246/cl.170989.
[32] A. Beck, G. Magesh, B. Kuppan, Z. Schay, O. Geszti, T. Benkó, R.P. Viswanath, P. Selvam, B. Viswanathan, L. Guczi, Specific role of polymorphs of supporting titania in catalytic CO oxidation on gold, Catal. Today 164 (2011) 325–331, https://doi.org/10.1016/j.cattod.2010.12.006.
[33] L. Di, D. Duan, X. Zhang, B. Qi, Z. Zhan, Effect of TiO_2 crystal phase and preparation method on the catalytic performance of Au/TiO_2 for CO oxidation, IEEE Trans. Plasma Sci. 44 (2016) 2692–2698, https://doi.org/10.1109/TPS.2016.2596784.
[34] I.N. Remediakis, N. Lopez, J.K. Nørskov, CO oxidation on rutile-supported Au nanoparticles, Angew. Chem. Int. Ed. 44 (2005) 1824–1826, https://doi.org/10.1002/anie.200461699.
[35] X. Bokhimi, R. Zanella, A. Morales, V. Maturano, C. Ángeles-Chávez, Au/rutile catalysts: Effect of the activation atmosphere on the gold-support interaction, J. Phys. Chem. C. 115 (2011) 5856–5862, https://doi.org/10.1021/jp111483v.
[36] A. Luengnaruemitchai, K. Srihamat, C. Pojanavaraphan, R. Wanchanthuek, Activity of Au/Fe_2O_3-TiO_2 catalyst for preferential CO oxidation, Int. J. Hydrog. Energy 40 (2015) 13443–13455, https://doi.org/10.1016/j.ijhydene.2015.07.148.
[37] K.M. Parida, N. Sahu, P. Mohapatra, M.S. Scurrell, Low temperature CO oxidation over gold supported mesoporous Fe-TiO_2, J. Mol. Catal. A: Chem. 319 (2010) 92–97, https://doi.org/10.1016/j.molcata.2009.12.005.

[38] M. Shou, H. Takekawa, D.-Y. Ju, T. Hagiwara, D.-l Lu, K.-i Tanaka, Activation of a Au/TiO_2 catalyst by loading a large amount of Fe-oxide: Oxidation of CO enhanced by H_2 and H_2O, Catal. Lett. 108 (2006) 119–124, https://doi.org/10.1007/s10562-006-0048-4.

[39] X. Bokhimi, A. Morales, M. Aguilar, J.A. Toledo-Antonio, F. Pedraza, Local order in titania polymorphs, Int. J. Hydrog. Energy 26 (2001) 1279–1287, https://doi.org/10.1016/S0360-3199(01)00063-5.

[40] X. Bokhimi, A. Morales, F. Pedraza, Crystallography and crystallite morphology of rutile synthesized at low temperature, J. Solid State Chem. 169 (2002) 176–181, https://doi.org/10.1016/S0022-4596(02)00046-4.

[41] F.J. Méndez, A. Herrera-González, A. Morales, X. Bokhimi, A novel approach for low-temperature synthesis of nanostructured rutile-like $Ti_{1-x}Fe_xO_2$ solid solutions, RSC Adv. 14 (2024) 28301–28307, https://doi.org/10.1039/D4RA03274H.

[42] R. Zanella, S. Giorgio, C.R. Henry, C. Louis, Alternative methods for the preparation of gold nanoparticles supported on TiO_2, J. Phys. Chem. B 106 (2002) 7634–7642, https://doi.org/10.1021/jp0144810.

[43] F.J. Méndez, A. González-Millán, J.A. García-Macedo, A new insight into Au/TiO_2-catalyzed hydrogen production from a water-methanol mixture using lamps containing simultaneous ultraviolet and visible radiation, Int. J. Hydrog. Energy 44 (2019) 14945–14954, https://doi.org/10.1016/j.ijhydene.2019.04.131.

[44] R.E. Dinnebier, A. Leineweber, J.S.O. Evans, Rietveld refinement: Practical powder diffraction pattern analysis using TOPAS, De Gruyter, Germany, 2019.

[45] R. Zanella, S. Giorgio, C.-H. Shin, C.R. Henry, C. Louis, Characterization and reactivity in CO oxidation of gold nanoparticles supported on TiO_2 prepared by deposition-precipitation with NaOH and urea, J. Catal. 222 (2004) 357–367, https://doi.org/10.1016/j.jcat.2003.11.005.

[46] S. Seritan, C. Bannwarth, B.S. Fales, E.G. Hohenstein, C.M. Isborn, S.I.L. Kokkila-Schumacher, X. Li, F. Liu, N. Luehr, J.W. Snyder, Jr, C. Song, A.V. Titov, I. S. Ufimtsev, L.-P. Wang, T.J. Martínez, TeraChem: A graphical processing unit-accelerated electronic structure package for large-scale ab initio molecular dynamics, WIREs Comput. Mol. Sci. 11 (2021) e1494, https://doi.org/10.1002/wcms.1494.

[47] G. Bussi, T. Zykova-Timan, M. Parrinello, Isothermal-isobaric molecular dynamics using stochastic velocity rescaling, J. Chem. Phys. 130 (2009) 074101, https://doi.org/10.1063/1.3073889.

[48] M.J. Frisch, G.W. Trucks, H.B. Schlegel, G.E. Scuseria, M.A. Robb, J.R. Cheeseman, G. Scalmani, V. Barone, G.A. Petersson, H. Nakatsuji, X. Li, M. Caricato, A.V. Marenich, J. Bloino, B.G. Janesko, R. Gomperts, B. Mennucci, H.P. Hratchian, J.V. Ortiz, A.F. Izmaylov, J.L. Sonnenberg, D. Williams-Young, F. Ding, F. Lipparini, F. Egidi, J. Goings, B. Peng, A. Petrone, T. Henderson, D. Ranasinghe, V.G. Zakrzewski, J. Gao, N. Rega, G. Zheng, W. Liang, M. Hada, M. Ehara, K. Toyota, R. Fukuda, J. Hasegawa, M. Ishida, T. Nakajima, Y. Honda, O. Kitao, H. Nakai, T. Vreven, K. Throssell, J.A.J. Montgomery, J.E. Peralta, F. Ogliaro, M.J. Bearpark, J. J. Heyd, E.N. Brothers, K.N. Kudin, V.N. Staroverov, T.A. Keith, R. Kobayashi, J. Normand, K. Raghavachari, A.P. Rendell, J.C. Burant, S.S. Iyengar, J. Tomasi, M. Cossi, J.M. Millam, M. Klene, C. Adamo, R. Cammi, J.W. Ochterski, R.L. Martin, K. Morokuma, O. Farkas, J.B. Foresman, D.J. Fox, Gaussian 16, Rev. C.02, Gaussian, Inc., Wallingford CT, 2016.

[49] International Center for Diffraction Data, X′pert HighScore Plus software v.3.0 PANalytical, PDF-2 database, Almelo, Netherlands.

[50] R. Camposeco, R. Zanella, Catalytic behavior of gold nanoparticles supported on a TiO_2-Al_2O_3 mixed oxide for CO oxidation at low temperature, Environ. Sci. Pollut. Res. 29 (2022) 76992–77006, https://doi.org/10.1007/s11356-022-21076-2.

[51] H.M. Tasdemir, The catalytic activity enhancement of commercial TiO_2 and Nb_2O_5 catalysts by iron for elemental sulfur production from H_2S, Catal. Lett. 149 (2019) 473–485, https://doi.org/10.1007/s10562-018-2634-7.

[52] M. Hinojosa-Reyes, R. Camposeco-Solis, R. Zanella, V. Rodríguez-González, F. Ruiz, Gold nanoparticle: Enhanced CO oxidation at low temperatures by using Fe-doped TiO_2 as support, Catal. Lett. 148 (2018) 383–396, https://doi.org/10.1007/s10562-017-2260-9.

[53] J. Bak, S. Clausen, Signal-to-noise ratio of FT-IR CO gas spectra, Appl. Spectrosc. 53 (1999) 697–700, https://doi.org/10.1366/0003702991947135.

[54] B. Schumacher, V. Plzak, M. Kinne, R.J. Behm, Highly active Au/TiO_2 catalysts for low-temperature CO oxidation: Preparation, conditioning and stability, Catal. Lett. 89 (2003) 109–114, https://doi.org/10.1023/A:1024731812974.

[55] P. Konova, A. Naydenov, C. Venkov, D. Mehandjiev, D. Andreeva, T. Tabakova, Activity and deactivation of Au/TiO_2 catalyst in CO oxidation, J. Mol. Catal. A: Chem. 213 (2004) 235–240, https://doi.org/10.1016/j.molcata.2003.12.021.